

Development of High-Efficiency *n*-Type Front and Back Contact Passivated Emitter and Rear Locally Diffused Solar Cells Using Atmospheric Pressure Chemical Vapor Deposition of Phosphosilicate Glass and Laser Processing

Xia Yan,* Ning Chen, Firdaus Bin Suhaimi, Xinyu Zhang, Qi Wang, Hao Jin, Vinodh Shanmugam, and Shubham Duttagupta

Industrial bifacial *n*-type front and back contact (*n*FAB) silicon solar cells, consisting of a boron-doped p^+ emitter and a phosphorus-doped n^+ back surface field (BSF), are known to give good bifaciality, high and stabilized efficiency. One possible approach to further enhance the cell efficiency is to convert conventional passivated emitter and rear totally diffused (PERT) into rear locally diffused (PERL) structure. Herein, bifacial *n*FAB PERT and PERL cells are fabricated by combining atmospheric pressure chemical vapor deposition (APCVD) of phosphosilicate glass (PSG) as doping source and laser processing. For PERL cells, two approaches are studied to locally form phosphorus-doped BSF: 1) laser doping, and 2) laser ablation of a diffusion barrier layer. For ablation approach, an alkaline treatment is introduced immediately after laser process, which leads to the formation of locally textured BSF. Due to this locally textured contact, the resultant fill factor (*FF*) and series resistance (R_s) loss of the PERL cells are even less than that of the reference PERT cells. As a result, the champion cell of PERL shows a good efficiency of 21.3% with open-circuit voltage (V_{oc}) of 662 mV, short-circuit current density (J_{sc}) of 39.6 mA cm^{-2} , and a high *FF* of 81.1%.

bifaciality.^[1–3] Typical bifacial *n*-type mono-Si solar cells, known as front and back contact (*n*FAB) cells at SERIS,^[4] adapt the passivated emitter and rear totally diffused (PERT) $p^+ - n - n^+$ structure,^[5] with the use of a full area phosphorus-doped back surface field (BSF).^[6–8] Currently, three types of diffusion techniques/tools are available for BSF formation: tube diffusion using phosphoryl chloride (POCl_3), ion implantation, and atmospheric pressure chemical vapor deposition (APCVD). Among these, POCl_3 diffusion is widely used in both production and research laboratory as it is the most mature process, but it usually requires a mask layer as diffusion barrier on the boron side.^[9] In contrast, ion implantation is able to produce accurate single-side doping with high uniformity, but it requires mandatory thermal treatments to anneal out the defects caused by these energetic ions.^[10–12] Compared

1. Introduction

Nowadays *n*-type monocrystalline silicon (mono-Si) solar cells are becoming more important for photovoltaic (PV) industry due to their high-efficiency potential and inherently good

with implantation, APCVD is another single-side deposition method, considered as an economical, simple and easy-to-maintain, and potentially well suited for large-scale industrial applications.^[13–15] In our previous work, we have optimized the APCVD process and demonstrated comparable *n*FAB cell efficiencies achieved via this mask-free method.^[16]


Due to the use of a full area heavily doped BSF layer, the performance of *n*FAB PERT cells is largely limited due to a high recombination velocity at rear surface.^[17] How to improve rear side passivation becomes one key point to improve the cell efficiency. One feasible approach is to confine the BSF locally diffused only beneath the metal contacts, namely, the so-called passivated emitter and rear locally diffused (PERL) structure.^[18–20] Under this concept, a world-record cell efficiency of 25.0% was achieved using a small area (4 cm^2) *p*-type silicon substrate.^[21,22] Similarly, a high efficiency 23.9% was also reported on an *n*-type aperture cell (4 cm^2).^[23] However, both approaches involve the use of high purity float zone (FZ) silicon substrates, photolithography, and non screen-printed metallization, which is not economical for industrial mass production.

In this work, we continue the fabrication studies of bifacial *n*FAB solar cells with the use of APCVD for phosphorus BSF

Dr. X. Yan, N. Chen, F. Bin Suhaimi, Dr. V. Shanmugam, Dr. S. Duttagupta
Solar Energy Research Institute of Singapore
National University of Singapore
7 Engineering Drive 1, 117574 Singapore, Singapore
E-mail: xiayan@nus.edu.sg

N. Chen
Photovoltaic Materials and Devices
Delft University of Technology
Mekelweg 4, 2628 CD Delft, The Netherlands

Dr. X. Zhang, Dr. Q. Wang, Dr. H. Jin
Jiaxing Key Laboratory of Advanced Photovoltaic Materials
Zhejiang Jinko Solar Co. Ltd
No. 58 Yuanxi Road, Yuanhua Industrial Zone, Haining 314416, Zhejiang, China

 The ORCID identification number(s) for the author(s) of this article can be found under <https://doi.org/10.1002/pssa.202000117>.

DOI: 10.1002/pssa.202000117

formation. We first vary the APCVD dopant contents and study the laser doping process. Adopting APCVD layer as dopant source allows the possibility of varying dopant profiles, independent of the laser process. Based on optimized APCVD condition, we fabricated and compared three types of bifacial *n*FAB cells of rear totally diffused (PERT), or locally diffused BSF (PERL) structure. The PERL cells were prepared using either laser doping or an alternative laser ablation method. All the fabrication processes were performed using industrial manufacturing facility and feasible technology, using 6 in. large area (M2 size, 244.32 cm²) *n*-type Czochralski (Cz) grown silicon wafers.

2. Experimental Section

2.1. Atmospheric pressure chemical vapor deposition

In this work, we used an inline APCVD system (5K6 Series, Schmid Thermal Systems) that was designed to uniformly deposit SiO_x (doped or intrinsic) films onto various substrates. This tool utilized a conveyor belt to transport the substrates through preheat, deposition, and cooling processing stages. During the deposition stages, the wafers/substrates moved through successive, independently controlled coating chambers. After processing, the substrates were unloaded from the continuously moving conveyor belt, where the belt was cleaned during its return to the load end of the system by an in situ continuous belt cleaning system.

For phosphosilicate glass (PSG) deposition, the chemical precursors for the SiO₂ film were SiH₄ and O₂, whereas phosphine (PH₃) was used as phosphorus dopant source. During deposition, the silicon wafers were preheated to around 600 °C before they interacted with the reactant gases delivered through CVD injectors. An inert gas (separator N₂) was used to maximize the surface reaction. During process, PH₃ and SiH₄ reacted with O₂ following Equation (1) and (2), and SiO₂ and P₂O₅ mixture to form a layer of PSG. The H₂ and H₂O were by-products of the reaction and were exhausted. Same gases except the doping gases (PH₃) were used to grow a nondoped SiO_x capping layer on top of the PSG.



Due to the gas flows, some minor wrap-around at the edges of the wafers were expected, as shown in Figure 1a, which could be

easily removed by a quick hydrofluoric acid (HF) dip at room temperature (RT). After APCVD deposition, a thermal annealing was conducted within a standard industrial tube diffusion furnace (Quantum, Tempress B.V.). The annealing process consisted of two stages, namely, thermal drive-in (DI) at 840 °C for 20 min in a pure N₂ ambient and post oxidation (PO) at 845 °C for 20 min, as shown in Figure 1b. The high temperature forced the phosphorus dopants to out-diffuse from PSG layer and driven into the silicon, whereby forming *n*⁺ BSF. Afterward the PO helped to tailor the dopant profile while reducing inactive dopants.

2.2. Characterization

To characterize the electrical properties, samples with specific laser patterns were prepared by doping within a 5 × 5 cm² square pad window on dedicated *p*-type silicon wafers. We measured the sheet resistance (*R*_{sheet}) of the doped layer using a mapping four-point probe (4pp; SR2000N, AIT Instruments). In addition, the dopant profile, such as junction depth and surface concentration, also played an essential role in determining the BSF quality and contactability to the metal grids. An electrochemical capacitance–voltage (ECV) profiler (WEP CVP21) was used to measure the electrically active phosphorus dopant profile.

In terms of solar cell performance, the current–voltage (*I*–*V*) characteristics were recorded by a flash solar simulator (SINUS220, Wavelabs) based on light-emitting diodes (LEDs). A reflective and conductive copper chuck was used for the measurement. Prior to *I*–*V* measurement, the light intensity of the simulated AM1.5G solar spectrum had been calibrated based on a reference cell, whereby also compensating the shading errors caused by probe bars.^[24]

3. Results and Discussion

3.1. Laser Doping Studies

Compared with conventional tube-based POCl₃ diffusion, the use of APCVD provides high freedom and convenience for tailoring phosphorus concentration of the deposited PSG layer. In previous work, we have systematically studied the influence of APCVD phosphorus contents on sheet resistance and saturation current density of the BSF layer.^[16] And a *R*_{sheet} in the range of 70–80 Ω sq^{−1} is identified as a suitable doping level of BSF layer for fabricating *n*FAB PERT solar cells.^[6,16]

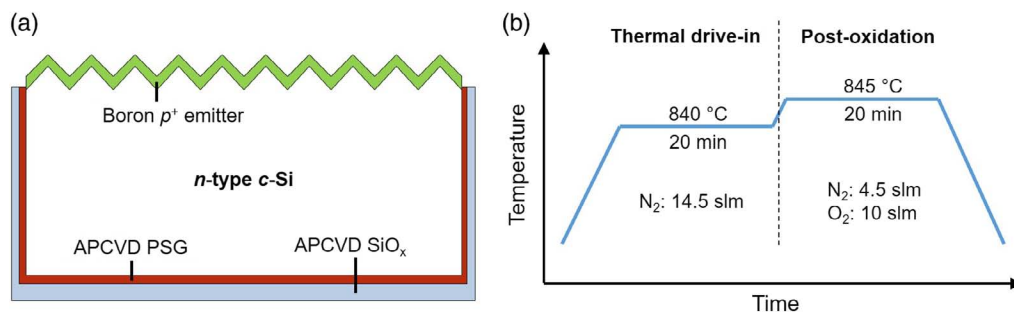


Figure 1. Schematic of a) a sample structure, and b) the thermal annealing process for APCVD PSG.

This work investigates the impact of APCVD PSG concentration for laser doping process. We vary the PH_3 /hydride ratio from 24 to 36, 45 and 50 mol%, and the resultant phosphorus content of PSG film changes from ≈ 12 to 18, 22.5 and 25 wt% (weight percentage). As the PSG layer is sensitive to the humidity, we performed laser doping immediately after APCVD process. The utilized Nanio laser source of the laser system (ILS500LT, InnoLas) produces nanosecond pulses with a central wavelength (λ) of 532 nm. We vary the nanosecond laser frequency from 40 to 100 and 200 kHz while using preoptimized laser power at each frequency and a constant scan rate of 0.5 m s^{-1} , which corresponds to laser fluence of 5.3, 3.2, and 3.1 J cm^{-2} , respectively.

Figure 2a shows the variations of sheet resistance value of laser-doped region of APCVD PSG layer, as a function of phosphorus content, obtained at three different nanosecond laser frequencies. A higher PSG concentration does not necessarily correspond to a lower R_{sheet} after laser doping. Instead, the overall trend indicates lowest R_{sheet} values achieved with the use of 18 wt% PSG, regardless of the laser frequency. In terms of laser pulse, the use of 40 kHz laser (i.e., a longer pulse) causes more ablation instead of doping, and thus results in a higher R_{sheet} value. The doping results are similar between 100 and 200 kHz laser, considering almost the same fluence used. For cell fabrication, we have chosen

100 kHz laser for doping of PSG layer because it results in a sufficient low R_{sheet} value of $\approx 22 \Omega \text{ sq}^{-1}$. We also conducted a post laser thermal annealing (condition as discussed in Section 2.1) to minimize laser-induced damages. This annealing treatment slightly tailors the dopant profile and further reduces the R_{sheet} to $18 \Omega \text{ sq}^{-1}$, as shown in **Figure 2b**.

3.2. Solar Cell Fabrications

Based on the obtained APCVD and laser doping results, we fabricate three types of bifacial nFAB solar cells with split 1) full area homogenous n^+ BSF, split 2) locally n^+ BSF via laser-doping, and split 3) locally textured n^+ BSF via laser-ablation. **Figure 3** shows the schematic structures of the three types of nFAB solar cells. All three cells have the same p^+ homogeneous emitter, passivation stack, and metal grids, with only difference in the BSF layer.

Figure 4 shows the fabrication process flow of each cell structure. To start, n -type raw wafers ($180 \mu\text{m}$, $\approx 2 \Omega \text{ cm}$) were saw-damaged etched (SDE) and double-side alkaline textured, followed by a standard Radio Corporation of America (RCA) cleaning and HF dip. The front p^+ emitter formed via boron tribromide (BBR_3) diffusion. During diffusion, wafers were back-to-back loaded to minimize rear-side wrap-around. The used

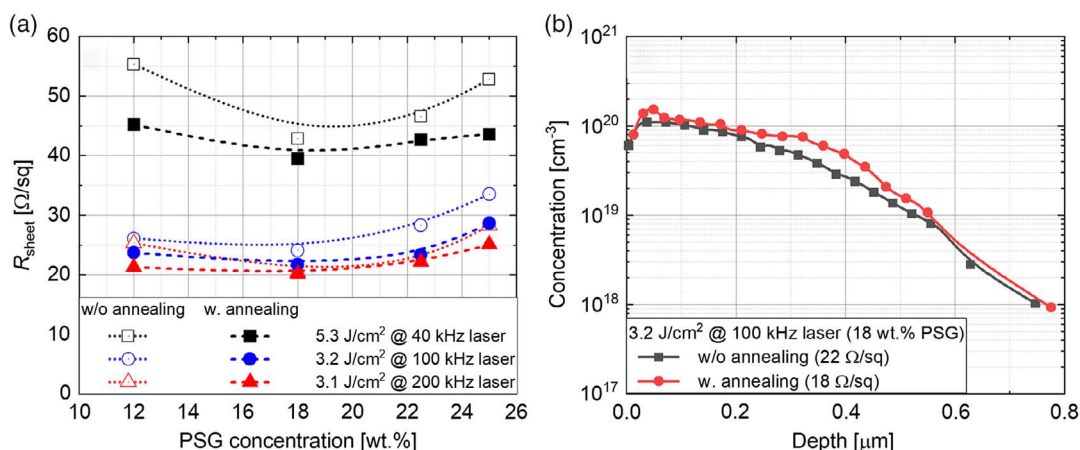


Figure 2. a) Variations of R_{sheet} values of laser-doped regions on APCVD PSG layer, as a function of phosphorus content. b) Variations of selected ECV profiles before and after thermal annealing.

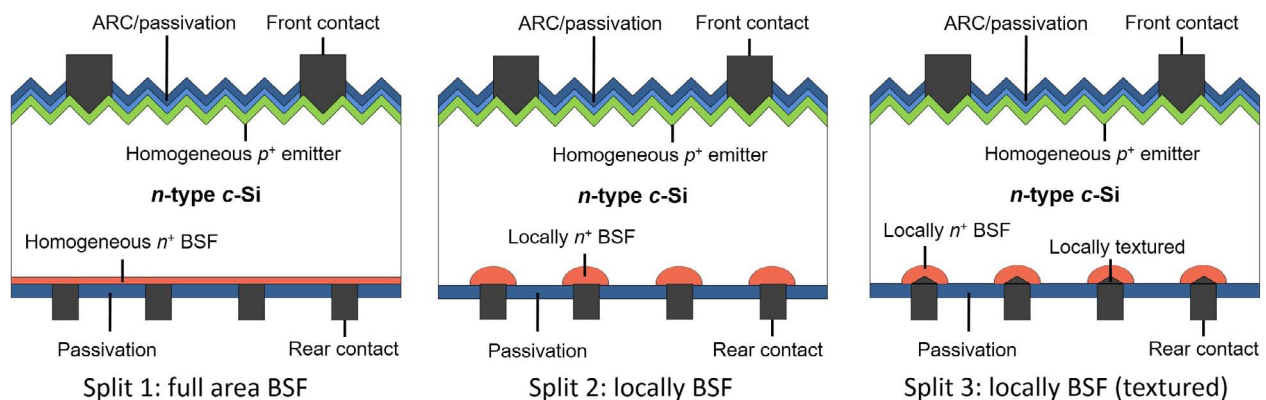


Figure 3. Schematic structures of bifacial nFAB PERT and PERL solar cells.

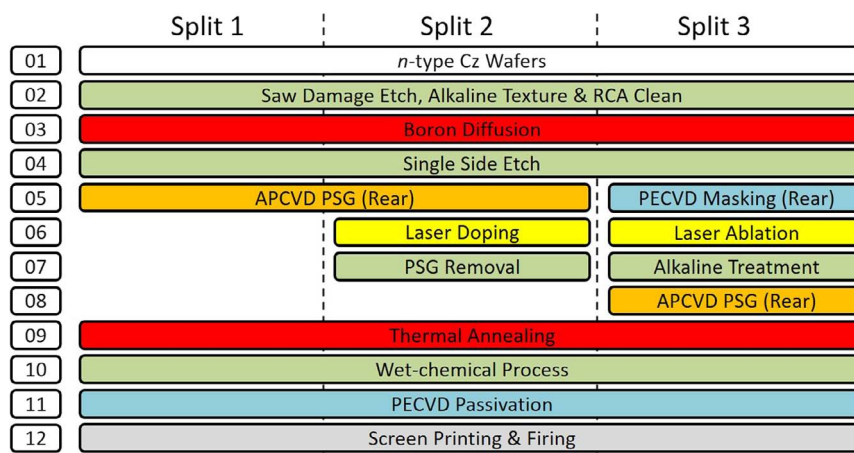


Figure 4. Schematic fabrication process flow of bifacial nFAB PERT and PERL solar cells by use of APCVD PSG and relevant laser processing techniques.

preoptimized boron diffusion produces a low saturation current density (J_{0e}) of $35 \pm 5 \text{ fA cm}^{-2}$ for homogeneous p^+ emitter with an average R_{sheet} of $\approx 85 \Omega \text{ sq}^{-1}$.

After single-side etch process (SSE; i.e., step 4), we divided wafers into three groups. A uniform PSG layer (18 wt% concentration) with SiO_x capping was deposited by APCVD at rear-side of the wafers for both split 1 and 2. The samples of split 1 immediately went for a high temperature ($>800^\circ\text{C}$) thermal annealing process, whereby forming a full-area n^+ BSF layer. In contrast, the APCVD layer was used as phosphorus dopant source for laser-doping samples of split 2 (i.e., step 6). To achieve local BSF, the PSG layer was stripped by an HF dip (i.e., step 7) prior to the thermal annealing.

An alternative laser ablation method was applied for samples of split 3. A dielectric masking layer of $\text{SiO}_x/\text{SiN}_x$ stack (60/120 nm) was applied to the rear-side of the wafers (i.e., step 5) to act as the diffusion barrier layer (i.e., step 9). Laser was used to selectively open the rear dielectrics. An additional wet-chemical alkaline treatment (i.e., step 7, retexturing for 5 min) process was introduced after the laser ablation, which is supposed to reduce laser-induced damages (by etching away damaged regions) and meanwhile roughens the silicon surface. This application of roughed silicon surface at the rear side is known for better ohmic contact (i.e., reduced metal-silicon contact resistance) and also enhances the bifaciality of nFAB solar cells.^[25] After the alkaline treatment, a PSG layer was deposited on top of the patterned dielectric mask layer by APCVD. During the thermal annealing, the phosphorus dopants can only diffuse into the bulk c -Si via these ablated regions, whereby forming locally n^+ doped BSF along texture morphology.

The value of R_{sheet} represents the lateral electrical conductivity of doped layer. The thermal annealing gives around $79 \Omega \text{ sq}^{-1}$ for full-area BSF (i.e., split 1) and $87 \Omega \text{ sq}^{-1}$ for locally textured BSF (i.e., split 3). In contrast, the optimized laser doping process produces a very low R_{sheet} of $\approx 18 \Omega \text{ sq}^{-1}$ (i.e., split 2). **Figure 5** compares the corresponding three phosphorus dopant profiles measured via ECV. Laser can easily drive the phosphorus dopants deep into the c -Si bulk. And thus a much heavier and deeper junction ($>0.8 \mu\text{m}$) was obtained for split 2. The texture

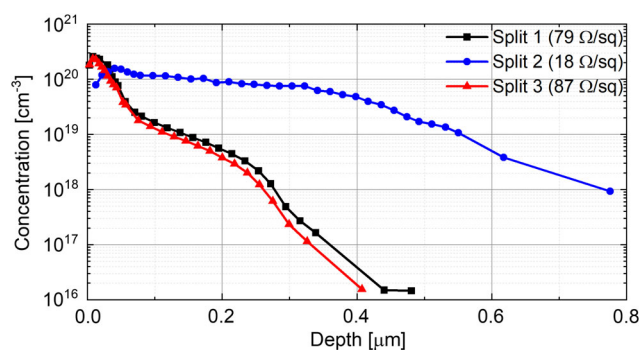


Figure 5. ECV dopant profiles of n^+ BSF for three types of solar cells.

morphology slightly lightens the dopant level of split 3, as compared with that of split 1's smoother surface.

After BSF formation, all the wafers were wet-chemical cleaned and then passivated at the same time by use of an inline plasma-enhanced chemical vapor deposition (PECVD) reactor (MAiA 2.1, Meyer Burger). A SiN_x layer of $\approx 75 \text{ nm}$ was applied to cap the n^+ BSF at rear-side, whereas an $\text{AlO}_x/\text{SiN}_x$ stack (20/50 nm) was used for passivating front p^+ emitter. Then all the cells were metallized by standard five-busbar (5BB, each $0.5 \mu\text{m}$ wide) grids in an industrial screen print tool (PVD1200, DEK). The metal grids consist of 125 Ag fingers at rear-side, whereas 87 Ag-Al fingers at front-side. A rapid thermal process was done to fire through the pastes and form good ohmic contact, in an inline fast firing belt furnace (SinTerra, BTU). The optical microscope images (Zeta microscopy) shown in **Figure 6** is an example of laser drive-in PSG areas aligned with metallized fingers, measured at several points across the whole wafer. Ideally, the locally n^+ BSF should be applied only underneath the intended area for rear fingers of the solar cells. The metal finger grids align well with the laser pattern in the middle region of the cells. But the alignment tends to gradually deteriorate toward wafer edges and corners. Moreover, there is some wafer to wafer variations. Due to the equipment limitation, we have to use a very wide laser pattern ($\approx 270 \mu\text{m}$ line, corresponding to

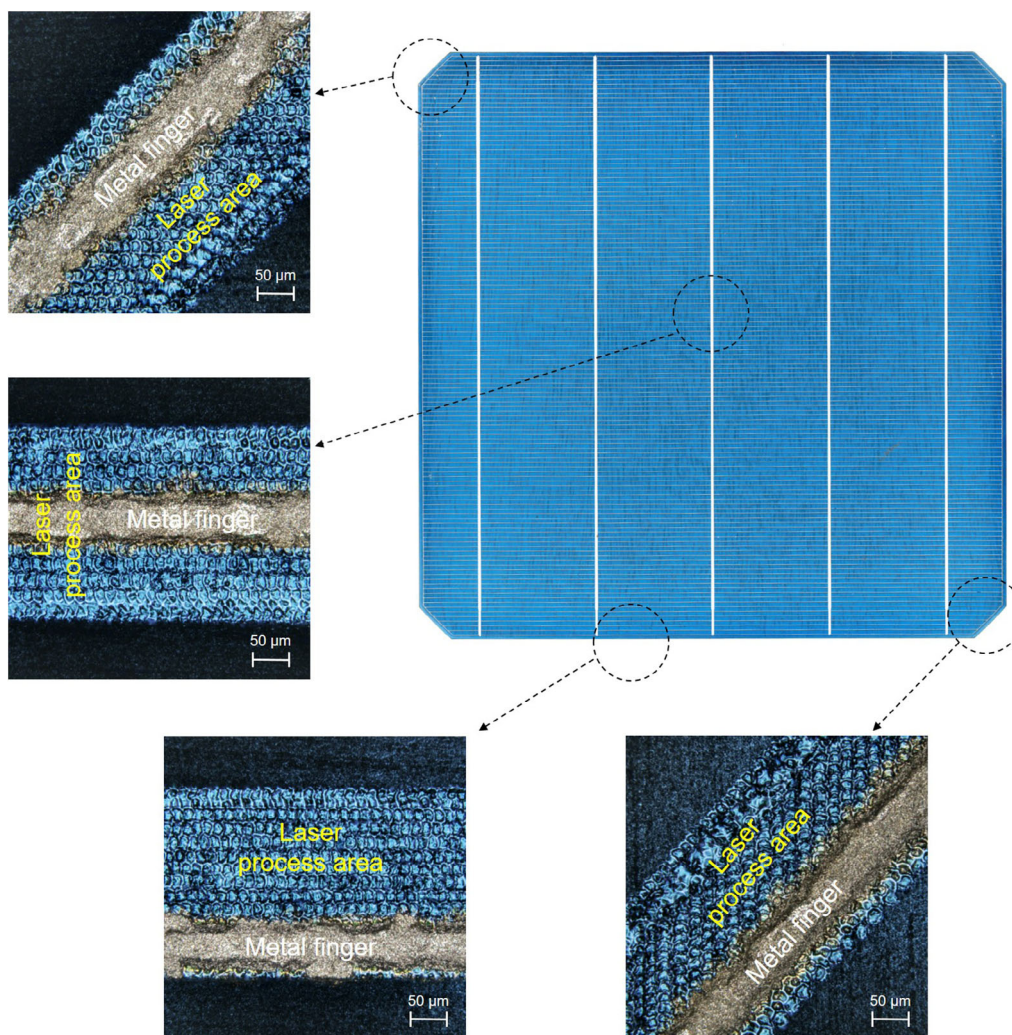


Figure 6. Optical images of laser drive-in BSF areas aligned with metallized finger grids, measured at several spots over the wafer.

$\approx 22\%$ of total area) to achieve good alignment to the printed metal finger width ($\approx 60 \mu\text{m}$, corresponding to $\approx 5\%$ of total area) over the whole batch fabrication.

Figure 7 compares the I - V data and **Table 1** shows the results of the obtained bifacial n FAB solar cells. With regard to batch average efficiency (η), there is little difference between cells of split 1 and 3, all around 20.9% efficiency with similar distribution spreads. However, the PERL cells of split 2 suffer from both lower open-circuit voltage (V_{oc} , ≈ 2 –3 mV) and fill factor (FF , $\approx 1.5\%$), and thus a lower efficiency of 20.3%. This inferior performance is mainly associated with the laser damages.

In contrast, the rear-side alkaline retexturing treatment (introduced in process step 7 of split 3) helps to greatly reduce the loss due to series resistance (R_s of $\approx 0.25 \Omega \text{cm}^2$). The local contact resistance ($R_{\text{c, rear}}$) between the n^+ BSF and rear fingers, measured by transmission line measurement (TLM), drops from around 1.38 to 0.27 $\text{m}\Omega \text{cm}^2$ by turning SSE surface into locally textured morphologies. As a result, the FF of PERL cells is $\approx 0.5\%$ higher than that of the PERT cells of split 1. A champion cell efficiency of 21.3% and $V_{\text{oc, max}}$ of 662 mV is obtained from split 3.

Due to equipment limitation, we still have several metal finger misalignments found on one of the PERL cell from split 3, even with the use of $\approx 270 \mu\text{m}$ wide locally BSF. And this particular inferior performance cell gives a low V_{oc} below 650 mV and a low FF of 80%, and thus only $\approx 20.2\%$ efficiency. The use of wider laser processed lines is one main bottleneck for the efficiency improvement in this work, due to the introduction of non-necessarily extra laser damage and heavy doping to the solar device. Therefore, we expect that the n FAB PERL cells will deliver better V_{oc} and efficiency if good alignment achieved on a narrower laser processed area.

To further study the contact resistance on planar and textured wafers, we performed cross-sectional scanning electron microscopy (SEM; Auriga, Carl Zeiss) analysis, as shown in **Figure 8**. On single-side etched wafer, we could observe a laterally continuous interfacial glass layer (in between the bulk Ag and the phosphorus doped silicon surface) (see **Figure 8a**). In contrast, as can be seen in **Figure 8b**, the retextured wafer surface results in more direct contact between the Ag finger and the Ag crystallites grown in to the phosphorus-doped Si surface, thus results in an excellent FF of close to 81.0% for the n PERL batch cells.

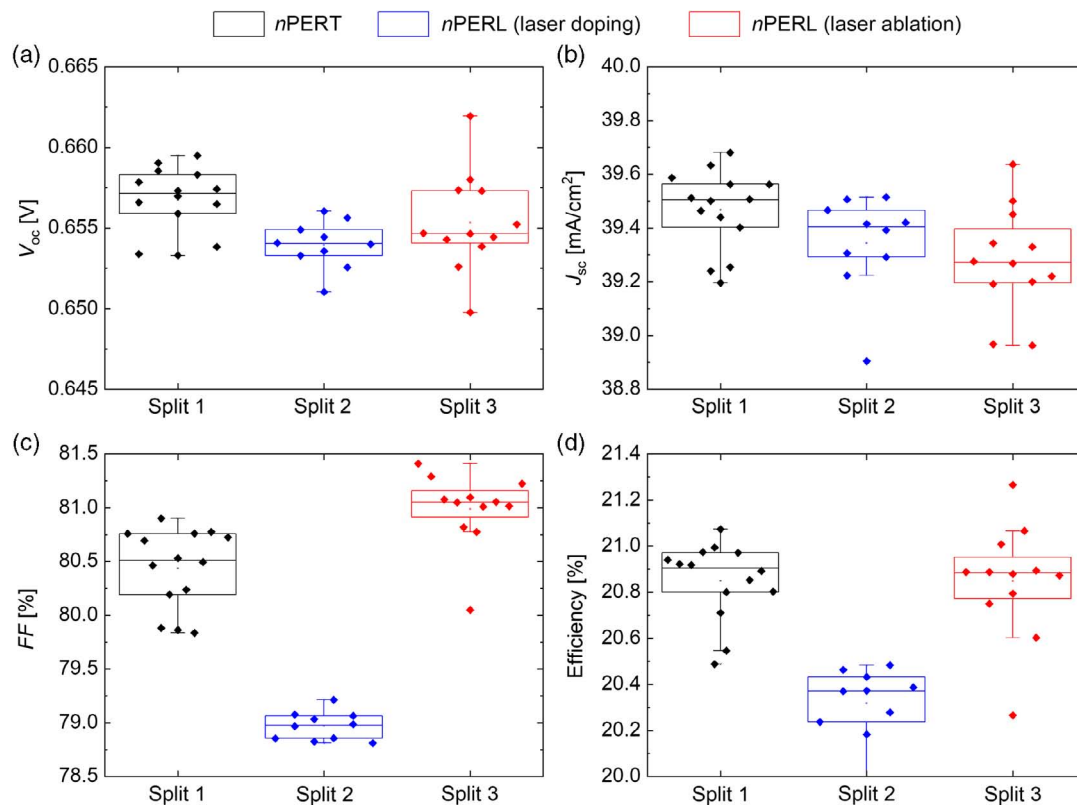


Figure 7. Box plots of a) open-circuit voltage, b) short-circuit current density, c) fill factor, and d) efficiency of bifacial *n*FAB PERT and PERL solar cells.

Table 1. Summary of *I*–*V* results, series, and rear side contact resistances of *n*FAB PERT and PERL solar cells.

Cell type	V_{oc} [mV]	J_{sc} [mA cm^{-2}]	FF [%]	η [%]	R_s [$\Omega \text{ cm}^2$]	$R_{c, rear}$ [$\text{m}\Omega \text{ cm}^2$]	$V_{oc, max}$ [mV]	η_{max} [%]
Split 1 (PERT)	657	39.47	80.44	20.9	0.34	0.57	659	21.1
Split 2 (PERL, laser-doping)	654	39.34	78.97	20.3	0.80	1.38	656	20.5
Split 3 (PERL, laser-ablation)	655	39.28	80.99	20.9	0.25	0.27	662	21.3

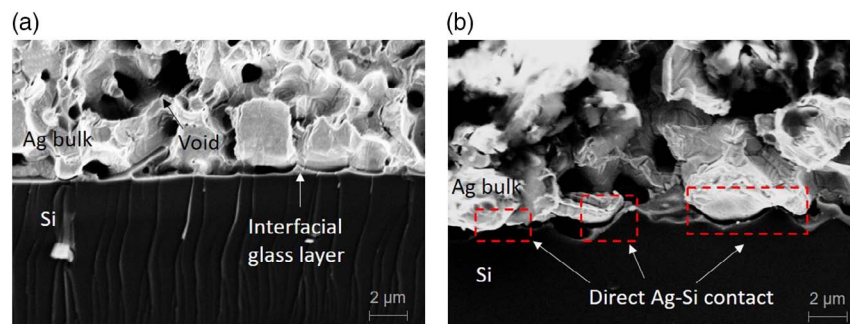


Figure 8. Cross-sectional SEM images of silver-silicon contact area for single-side etched wafers a) without additional alkaline treatment, and b) after 5 min alkaline treatment.

4. Conclusions

This work focuses on the development of bifacial *n*FAB PERL cells via either laser doping or laser ablation approach. We make use of and study APCVD-deposited PSG as the phosphorus

dopant source for n^+ BSF formation. We first investigate the influence of PSG concentration on laser doping process, for nanosecond green laser of different pulse frequencies. The effects of full area and locally BSF layers are validated based on the device performance of bifacial *n*FAB solar cells, fabricated

using all industrial feasible approaches on standard M2 size Cz monocrystalline silicon wafers. The obtained best *n*PERL cell gives a high *FF* of 81.1% together with V_{oc} of 662 mV and J_{sc} of 39.6 mA cm^{-2} , and conversion efficiency of 21.3%. We believe that the *n*FAB PERL cells will deliver better performance, provided good alignment can be achieved on a narrower laser processed area.

Acknowledgements

The Solar Energy Research Institute of Singapore (SERIS) is supported by the National University of Singapore (NUS) and Singapore's National Research Foundation (NRF) through the Singapore Economic Development Board (EDB). This research was supported by a joint research collaboration project, "Development of bifacial front and back contacted solar cells using monocrystalline silicon wafers," between Jinko Solar and SERIS. This work acknowledges the funding via the Key Project of Zhejiang Province (grant no. 2018C01034).

Conflict of Interest

The authors declare no conflict of interest.

Keywords

back surface field, chemical vapor deposition, passivated emitter, phosphosilicate glass, rear locally diffused structure, solar cells

Received: March 4, 2020

Revised: April 7, 2020

Published online: May 5, 2020

- [1] D. Song, J. Xiong, Z. Hu, G. Li, H. Wang, H. An, B. Yu, B. Grenko, K. Borden, K. Sauer, T. Roessler, J. Cui, H. Wang, J. Bultman, A. H. G. Vlooswijk, P. R. Venema, in *38th IEEE Photovoltaic Specialists Conf.*, Austin **2012**, pp. 3004–3008.
- [2] J. Liu, Y. Yao, S. Xiao, X. Gu, J. *Phys. D: Appl. Phys.* **2018**, *51*, 123001.
- [3] W. Cai, S. Yuan, Y. Sheng, W. Duan, Z. Wang, Y. Chen, Y. Yang, P. P. Altermatt, P. J. Verlinden, Z. Feng, *Energy Procedia* **2016**, *92*, 399.
- [4] J. Rodriguez, E.-C. Wang, N. Chen, J. W. Ho, M. Li, J. K. Buatis, B. Nagarajan, L. Xu, W. L. Choy, V. Shanmugam, J. Wong, A. G. Aberle, S. Duttagupta, *Sol. Energy Mater. Sol. Cells* **2018**, *187*, 91.
- [5] Y. Tao, K. Madani, E. Cho, B. Rounsaville, V. Upadhyaya, A. Rohatgi, *Appl. Phys. Lett.* **2017**, *110*, 021101.
- [6] X. Yan, E.-C. Wang, N. Chen, L. Zhang, X. Gong, X. Zhang, S. Duttagupta, *Sol. Energy* **2019**, *179*, 335.
- [7] S. Meier, S. Maier, C. Demberger, A. Wolf, D. Biro, S. W. Glunz, *Sol. RRL* **2017**, *1*, 1600005.
- [8] Q. Wei, S. Zhang, S. Yu, J. Lu, W. Lian, Z. Ni, *Energy Procedia* **2017**, *124*, 700.
- [9] T. Blévin, A. Lanterne, B. Grange, R. Cabal, J. P. Vilcot, Y. Veschetti, *Sol. Energy Mater. Sol. Cells* **2014**, *131*, 24.
- [10] J. Shi, X. Li, D. Song, W. Yang, F. Li, F. Lang, S. C. Pop, W. Zhang, J. Wang, B. Yu, *Sol. Energy* **2017**, *142*, 87.
- [11] K. Ryu, S. Kim, W. Kim, M. Shin, A. Cheng, Y. Shin, J. Whittemore, J. Garcia, K. Qureshi, K. Kim, B. Kim, in *43rd IEEE Photovoltaic Specialists Conf.*, IEEE, Piscataway, NJ **2016**, pp. 2512–2514.
- [12] Y. Tao, A. Payne, V. D. Upadhyaya, A. Rohatgi, *Prog. Photovoltaics* **2014**, *22*, 1030.
- [13] F. Book, H. Knauss, C. Demberger, F. Mutter, G. Hahn, in *32nd European Photovoltaic Solar Energy Conf. and Exhibition*, Curran Associates, Inc., Red Hook, NY **2016**, pp. 824–827.
- [14] S. Meier, S. Wiesnet, S. Mack, S. Lohmüller, S. Maier, S. Unmüßig, C. Demberger, H. Knauss, D. Biro, A. Wolf, in *32nd European Photovoltaic Solar Energy Conf. and Exhibition*, Curran Associates, Inc., Red Hook, NY **2016**, pp. 565–570.
- [15] P. Rothhardt, S. Meier, C. Demberger, A. Wolf, D. Biro, *Energy Procedia* **2014**, *55*, 287.
- [16] N. Chen, E.-C. Wang, X. Yan, V. Shanmugam, B. Nagarajan, L. Zhang, X. Gong, X. Zhang, Q. Wang, H. Jin, S. Duttagupta, *Phys. Status Solidi A* **2019**, *216*, 1900238.
- [17] A. Richter, J. Benick, A. Kalio, J. Seiffe, M. Hörteis, M. Hermle, S. W. Glunz, *Energy Procedia* **2011**, *8*, 479.
- [18] A. Blakers, N. Zin, K. R. McIntosh, K. Fong, *Energy Procedia* **2013**, *33*, 1.
- [19] C. Battaglia, A. Cuevas, S. De Wolf, *Energy Environ. Sci.* **2016**, *9*, 1552.
- [20] J. Benick, B. Steinhauser, R. Müller, J. Bartsch, M. Kamp, A. Mondon, A. Richter, M. Hermle, S. Glunz, in *40th IEEE Photovoltaic Specialist Conf.*, IEEE, Piscataway, NJ **2014**, pp. 3637–3640.
- [21] J. Zhao, A. Wang, A. Green Martin, *Prog. Photovoltaics* **2000**, *7*, 471.
- [22] M. A. Green, *Prog. Photovoltaics* **2009**, *17*, 183.
- [23] S. W. Glunz, J. Benick, D. Biro, M. Bivour, M. Hermle, D. Pysch, M. Rauer, C. Reichel, A. Richter, M. Rüdiger, C. Schmiga, D. Suwito, A. Wolf, R. Preu, in *35th IEEE Photovoltaic Specialists Conf.*, IEEE, Piscataway, NJ **2010**, pp. 50–56.
- [24] S. Raj, J. W. Ho, J. Wong, A. G. Aberle, *IEEE J. Photovoltaics* **2017**, *7*, 1203.
- [25] N. Chen, X. Yan, F. B. Suhaimi, L. Zhang, X. Gong, X. Zhang, S. Duttagupta, in *Light, Energy and the Environment 2018 (E2, FTS, HISE, SOLAR, SSL)*, Singapore **2018**, p. OT3C.3.